Identification of the mechanical behaviour and damage mechanisms of a Nextel™610/alumina ceramic matrix composite subjected to tensile loading

Camélia Ben Ramdane, Aurélie Julian-Jankowiak, Michel Parlier, Roger Valle, Eric Martin, Pascal Diss

Title: Identification of the mechanical behaviour and damage mechanisms of a Nextel™610/alumina ceramic matrix composite subjected to tensile loading.

Authors names and affiliations:

Camélia Ben Ramdane[a,b,c] (name: Camélia, last name: Ben Ramdane)

Aurélie Jankowiak[b] (name: Aurélie, last name: Jankowiak)

Michel Parlier[b] (name: Michel, last name: Parlier)

Roger Valle[b] (name: Roger, last name: Valle)

Eric Martin[d] (name: Eric, last name: Martin)

Pascal Diss[a] (name: Pascal, last name: Diss)

[a]Herakles, Rue de Touban, Les cinq chemins, 33185 Le Haillan, France

[b]Onera, 29 avenue de la Division Leclerc, 92322 Châtillon, France

[c]Université de Bordeaux, 351 Cours de la Libération, 33400 Talence

[d]Laboratoire des Composites Thermo-Structuraux, CNRS UMR 5801, Université de Bordeaux, 3 rue de La Boétie, 33600 Pessac, France

Corresponding author:

Camélia Ben Ramdane, benramdane.camelia@gmail.com phone number: 0033770339280

Abstract: (x ± y % = 4 words → counted as 1 , z % = 2 words → counted as 1 → total: < 150 words)

The present study was aimed at determining the mechanical behaviour of a weak matrix oxide/oxide CMC subjected to monotonic and cyclic tensile loading in fibre direction and in ±45° fibre orientation and at identifying the damage mechanisms. The material consisted of Nextel™610 fibres (8 HSW) embedded in an alumina matrix, with a fibre volume fraction of 49 % and 24 ± 2 % porosity. The average ultimate tensile stress and strain of the material were, respectively, 260 ± 37 MPa and 0.3 ± 0.09 % in fibre direction and 89 ± 19 MPa and 0.19 ± 0.07 % in ±45° fibre orientation. Interlaminar shear strength, evaluated through 3-point bending tests, was 20 ± 2 MPa. Various techniques were used for microstructural characterization of as-processed material. Two types of pores were differentiated within the material: micropores (13 ± 1 %) and macropores (12 ± 1 %). The latter appear to be the most

detrimental for the material, enhancing delamination. The damage mechanisms of the material were assessed through SEM examination and *in situ* tensile tests.

Keywords (4): A: Ceramic-matrix composites (CMCs), **B**: Fibre/matrix bond, **B**: Mechanical properties, **D:** Electron microscopy

Online submission/enter keywords: weak matrix

1. Introduction

Two solutions have risen to reduce aircraft greenhouse gases emissions: lightening the aircrafts and increasing the operating temperature of the gas turbine and, as a consequence, of the exhaust gases. Composite materials have been widely used during the last decades to reduce weight. Ceramic matrix composites (CMCs), used for thermostructural applications [1], fulfil both requirements: their density is lower than that of conventional nickel-based superalloys and they are capable of maintaining excellent strength and fracture toughness at high temperatures [2][3][4][5]. Moreover, these materials, designed for applications in oxidizing environments (turbo-engines), have to be oxidation-resistant and thermodynamically stable [2]. Non-oxide CMCs, generally SiC/SiC composites, show poor oxidation resistance at intermediate temperatures, around 700-800°C [3], due to the presence of carbon at the fibre/matrix interface.

Therefore, oxide fibre/oxide matrix CMCs appear to be good candidates for thermostructural applications in this temperature range [6]. Using oxide fibre/non-oxide matrix or non-oxide fibre/oxide matrix composites does not improve the high temperature oxidation resistance [3], the mechanical properties of the non-oxide components being reduced by oxidation. Despite their better oxidation resistance compared to SiC/SiC composites, oxide/oxide composites exhibit lower mechanical properties and cannot be used at temperatures higher than 1000-

1100°C. Beyond these temperatures, the degradation of the fibres [7] induces a decrease in the mechanical properties [8].

It is now commonly assumed that the mechanical performance of CMCs relies on the fibre/matrix interface. When matrix cracks initiate and propagate under loading, it seems necessary to isolate the fibres from the matrix so that they remain intact and ensure the mechanical strength of the composite [9]. Therefore, two approaches exist: weak matrix and weak interface composites [9][10][11]. The weak matrix approach is based on a microporous matrix. In these composites, cracks propagate between the micropores of the matrix, which enables energy dissipation, and, when matrix cracks reach the fibres, they are deflected at the fibre/matrix interface. This leads to fibre/matrix debonding and fibre pull-out, thereby providing high composite toughness [8][12]. The weak matrix concept assumes a strong fibre/matrix bond, but the high porosity of the matrix ensures a weak fibre/matrix interface. Weak matrix principle is illustrated in Fig. 1.

Regarding the second approach, it is based on a weak fibre/matrix interface promoting fibre/matrix debonding and sliding. This can be achieved by introducing a weak interphase between the fibres and the matrix, which is generally fully dense. Such an interphase consists of a fibre coating, which increases the process cost [12]. Thus, the weak matrix approach appears to be the most attractive. According to previous studies, the matrix porosity must be in the 30-40 % range to obtain a weak matrix composite [1][8][13]. Regarding the fibre volume fraction, it is essential, for turbo-engine applications, to manufacture materials with a high fibre volume fraction in order to enhance the mechanical properties of the composite material, especially the Young's modulus. Hence, the aimed fibre volume fraction and total porosity were 50 % [14] and 25 %, respectively.

Most of the oxide/oxide composites described in previous studies were reinforced with commercial Nextel™610 or Nextel™720 fibres embedded in an alumina, an alumina-silica or an alumina-mullite matrix. Nextel™610 alumina fibres offer high strength [12] at low and moderately high temperatures (up to approximately 1000°C) whereas Nextel™720 alumina-silica fibres have good creep resistance up to approximately 1200°C [8]. As for the matrix,

the main advantage of alumina compared to alumina-silica and alumina-mullite is that its sintering process can start at temperatures lower than 1000-1100°C. Beyond this temperature range, a loss of mechanical properties of Nextel™610 fibres occurs. Thus, combining Nextel™610 alumina fibres with an alumina matrix offers two advantages: *(i)* the matrix can be partially sintered without damaging the fibres and *(ii)* there is no reaction between fibres and matrix, hence avoiding the creation of a strong fibre/matrix interface that would prevent crack deflection at the fibre/matrix interface and therefore fibre debonding.

The objective of this study is to investigate the mechanical behaviour of a weak matrix alumina/alumina composite under tensile loading and to identify the damage mechanisms of this composite [15]. Previous studies on the mechanical behaviour of several oxide/oxide CMCs are available in the literature, but a precise description of the damage mechanisms of these composites seems to be absent.

Several techniques were used for the determination of damage mechanisms: optical microscopy and scanning electron microscopy examinations, *in situ* tensile testing in a scanning electron microscope (SEM), infrared thermography, X-ray tomography and ultrasonic scanning. None of the above damage monitoring techniques seems to be reported in the literature for an application to oxide/oxide CMCs.

2. Experimental procedure

2.1. Material

The material consisted of a micro-porous alumina matrix reinforced with woven Nextel™610 alumina fibres, without coating. The fibre fabric (8 harness satin weave) was first infiltrated with a water-based alumina matrix slurry, then dried and cut into twelve plies. These prepreg plies were then infiltrated with water, laid up in a mould, hot pressed at 100°C in a vacuum bag and finally heat treated at 1200°C (pressureless sintering) to obtain approximately 2.5 mm thick plates with the required microporosity and fibre volume fractions.

2.2. Mechanical testing and damage monitoring

In-plane mechanical properties of the Nextel™610/alumina composite were studied through uniaxial monotonic and cyclic loading in the fibre direction (weft direction) and in ±45° fibre orientation. All tests were conducted at room temperature in laboratory air environment, using a servocontrolled *Z150 Zwick/Roell Materials* testing machine. The tests were performed in stroke control with a constant displacement rate of 0.5 mm.min^{-1}.

Straight-sided specimens of 16 mm x 150 mm *x composite thickness*, with a gauge length of 70 mm were used [15].

Strain measurements were accomplished simultaneously by digital image correlation (DIC, *VIC-3D*™), a uniaxial extensometer of 25 mm gauge length (*Schenck*) and strain gauges (*Vishay Precision Group, CEA-06-250UW-350*). After test result analysis, it appeared that the uniaxial extensometer slid on the surface of the specimens. Besides, the strains measured by DIC and by strain gauges were very similar. Thus, only the strains measured by DIC were taken into account.

Young's moduli were determined from stress-strain curves and damage thresholds were defined as the stress and strain corresponding to the elastic limit, for each tested specimen.

In-plane shear moduli G_{xy} (GPa) were calculated through tensile tests performed on specimens with ±45° fibre orientation, using the following equation:

$$G_{xy} = \frac{F_{yy}}{2\ e\ l\ (\varepsilon_{yy} - \varepsilon_{xx})} \times 10^{-3} \quad (1)$$

where F_{yy} is the unidirectional force (N) applied in the loading direction, e and l are, respectively, the thickness (mm) and the width (mm) of the sample, ε_{yy} and ε_{xx} are, respectively, the longitudinal and transverse strains. Both longitudinal and transverse strains must remain within the elastic domain, according to the stress-longitudinal strain and stress-transverse strain curves.

For cyclic loading tests, the specimens were sequentially loaded at different stresses, with a return to zero load between two cycles. The sequential stresses were determined from monotonic tensile tests and correspond to different points on the stress-strain curves: a point slightly before the average damage threshold, a point just before the average failure and intermediate points. For 0° loading direction, the stresses were 23 %, 46 %, 69 % and 92 % of the average ultimate tensile stress of the material (*i.e.* 60 MPa, 120 MPa, 180 MPa and 240 MPa), while, for ±45° fibre orientation, the stresses were 17 %, 34 %, 51 %, 67 %, 84 % and 100 % of the average ultimate tensile stress (*i.e.* 15 MPa, 30 MPa, 45 MPa, 60 MPa, 75 MPa and 90 MPa).

Interlaminar properties are critical for laminated composites with 2D woven reinforcements. The interlaminar shear strength (ILSS) of the composite was measured by 3-point bending tests on short beams according to BS EN 658:5-2002 standard, in the fibre direction (0°). The schematic diagram of the 3-point bending test geometry is given in Fig. 2. The dimensions of ILSS test specimens were 25 mm x 10 mm x *composite thickness*. The cylindrical rollers had a diameter of 4 mm and the outer support span was 15 mm. A displacement rate of 0.5 mm.min^{-1} was used for these tests. The ILSS (MPa) is calculated using the following equation:

$$ILLS = \frac{3\,F}{4\,b\,h} \qquad (2)$$

where F is the shear failure force (N), b is the mean test specimen width (mm) and h is the mean test specimen thickness (mm).

In situ tensile tests were carried out in a SEM (*Zeiss DSM-960*) in order to *(i)* corroborate the *post mortem* observations and *(ii)* ascertain the chronology of the damage mechanisms. *In situ* testing offers two advantages: real time damage monitoring and observation of the material under load, which prevents crack closure when returning to zero load. This phenomenon cannot be avoided in the case of *post mortem* observation. But *in situ* testing also have disadvantages. First of all, the technique requires the use of small straight sided specimens (3 mm x 40 mm x *composite thickness*) with a 3 mm x 10 mm x *composite*

thickness gauge, which might not be representative of the macroscopic behaviour of the composite, the geometrical unit cell of the composite being 8 mm x 8 mm x *composite thickness*. Moreover, the observation of damage being performed on the specimen edge, the observed mechanisms are thus occurring in a plane stress state. The observed edge of the specimens was mirror polished prior to testing (without resin impregnation). The samples were observed in real-time during loading tests and images of the total gauge length were acquired after each 100 N loading step (approximately 13 MPa considering the section of the specimens), while the specimens were maintained under constant load.

2.3. Microstructural characterization

Porosity of the as-processed composite was measured by mercury intrusion porosimetry and by Archimedes' method, in water. The results obtained by these two techniques were similar. Five samples from five different plates were analysed.

The microstructure of the material was also studied through 3D computed tomography analysis. A *phoenix v|tome|x L300 (General Electric Sensing and Inspection Technologies)* X-ray tomograph was used for data acquisition, with a 180 kV source, enabling a 10.2 µm resolution. The scanned zone of the samples was approximately 21 mm x 16 mm x *composite thickness*.

In order to identify the damage mechanisms of the studied composites under tensile loading, SEM examination (*Zeiss DSM-962* and *Zeiss Gemini FEG-SEM*) were performed on as-processed and damaged composites (*post mortem* observations) [15]. The damaged composites consisted of specimens loaded at different stresses, *e.g.* 22 %, 59 %, 63 % and 85 % of the average ultimate tensile stress.

As for cyclic loading tests, these stresses were determined from monotonic tensile tests and correspond to different points on the stress-strain curves: a point slightly after the average damage threshold, a point just before the average failure point and two intermediate points. The gauge lengths of these specimens were observed to identify the damage mechanisms of

the composite. The observation of as-processed material and damaged specimens required a specific preparation. First, they were impregnated by an epoxy resin (in a vacuum chamber for a good impregnation of the microporosity), in order to *(i)* avoid further damaging of the samples during polishing and *(ii)* have a flat polished surface, the fibres and the matrix being equally polished. Then, the samples were cut in the middle planes, parallel and perpendicular to the loading direction (parallel and perpendicular to the fibres in the case of as-processed material). Finally, the obtained cross-sections were mirror polished for SEM observation.

In order to detect the possible manufacturing defects and to avoid using damaged plates, non-destructive inspections were performed, in transmission configuration, by infrared pulse thermography and ultrasonic scanning in immersion. The infrared camera used was a *CEDIP Jade LWIR (Long Wave InfraRed)* covering a 7-9 µm wavelength range, with a 20 mK noise equivalent temperature difference and a frequency acquisition of thermal images of 200 Hz. As for ultrasonic scanning technique, normalised transmitted energy maps were studied to detect damage. Two *Panametrics* transducers (*General ElectricSensing*) were used: *M309* type emission transducer and *V309* type reception transducer, with a 5 MHz nominal centre frequency. The plates were scanned with a 1 mm step, horizontally and vertically. Both non-destructive evaluation (NDE) methods enabled the detection of large defects, such as delamination. The pre-damaged areas of as-processed plates were removed. Only undamaged areas were used to extract testing samples.

Two non-destructive testing (NDT) methods have been used in this study for the determination of the damage threshold and for damage monitoring: passive infrared thermography and observation of the edge of the specimens by optical microscopy. In both cases, damage was detected at a very late stage, just before failure (for both 0° and ±45° loading directions).

3. Results and discussion

3.1. Microstructure

The total open porosity was 24 ± 2 %. The fibre volume fraction, deduced from the total porosity, was 49 %. The main advantage of mercury intrusion porosimetry compared to Archimedes' method is that it provides information about pore distribution (see Fig. 3). The composite exhibited two types of porosity: matrix microporosity and macroporosity. The limit between micro- and macroporosity was set at 0.1 µm. The microporosity, on which the weak matrix principle is based, was 13 ± 1 % of the total porosity of the composite and represented a volume fraction of 32 ± 1 % of the matrix. This fraction stands in the 30-40 % porosity range required for a weak matrix. The microporosity of the material is visible in the SEM micrograph presented in Fig. 4.a. The macroporosity was 12 ± 1 % of the total porosity of the composite. The macroporosity is due to a lack of matrix (see Fig. 4.b). The presence of macropores in oxide/oxide CMCs was reported in other studies [16] but not quantified. Fibre volume fraction and porosity data measured on the studied material are summarized in Table 1.

Concerning the macropores, two categories were identified: intraply and interply macropores. This distinction was assessed by means of X-ray tomography analysis and SEM observations, performed on as-processed materials. Approximately 65 % of the macroporosity, measured by analysis of X-ray tomography data, consisted in interply macropores whose distribution was heterogeneous. On the contrary, intraply macropores appeared to be randomly distributed. An example of X-ray tomography analysis is given in Fig. 5.

Besides macroporosity, as-processed materials exhibited matrix sintering shrinkage microcracks attributed to the sintering process (see Fig. 4.c). These cracks were predominantly normal to the direction of the woven reinforcement and concentrated in the

matrix-rich regions. The presence of sintering shrinkage cracks is common in CMCs and has been reported in several studies [1][3][8][9][10][17].

With regard to NDE techniques, the results obtained by infrared thermography and ultrasonic scanning were similar and showed that the plates were heterogeneous, some of them showing delaminated areas. This is in accordance with the previous observation by X-ray tomography pointing out the heterogeneous distribution of interply macroporosity. The example of a plate showing intensive delamination, identified by infrared thermography and ultrasonic scanning, is given in Fig. 6.

3.2. Mechanical properties

In-plane mechanical properties of the Nextel™610/alumina composite were studied through uniaxial monotonic and cyclic loading in the fibre direction (warp direction) and in ±45° fibre orientation. Uniaxial loading in the fibre direction provides information on the fibre-dominated properties whereas uniaxial loading in off-axis ±45° direction provides matrix-dominated properties. Nine specimens were cut from six different plates for monotonic tensile tests in the fibre direction and seven specimens were cut from three different plates for ±45° fibre orientation tests. For both directions, three specimens cut from different plates were used to perform cyclic tensile tests (three plates for the fibre direction tests and two plates for ±45° fibre orientation tests). As expected considering the heterogeneous microstructure of the material, curves and mechanical properties of the composite were scattered. Nevertheless, tensile curves exhibited the same shape for each direction of loading. The mechanical properties of the material are summarized in Table 2.

3.2.1. Mechanical properties in the fibre direction

Average ultimate tensile stress and strain of the composite are 260 ± 37 MPa and 0.30 ± 0.09 %, with a Young's modulus of 134 ± 19 GPa. The response of the studied composite under monotonic tensile loading in the fibre direction shows a first linear segment, a second quasi-linear segment and, in some cases, a third non-linear segment (see Fig. 7

and Fig. 8). The first linear segment constitutes the elastic region of the material. The damage threshold of the composite generally corresponds to the elastic limit. In most cases, the failure occurs at the end of the second quasi-linear segment. Such a behaviour, described as nearly linear up to failure, is common on oxide/oxide composites and has been reported by several authors [5][8][17][18]. However, in these studies, the slope of the second segment is slightly lower than the Young's modulus whereas, in the present case, the slopes of the first two segments are clearly different, as shown in Fig. 8.

The curved part of the tensile curves, between the elastic region and the second quasi-linear segment, indicates a brutal damage increase and can be considered as a damage threshold. The same assumption can be made regarding the non-linear third segment exhibited by some specimens. Young's modulus and maximum stress and strain of the studied composite are higher than those of all-oxide composites, reinforced with Nextel™610 fibres and with similar fibre volume fractions, reported in the literature [16][17][19]. However, the several all-oxide CMCs described do not exhibit the same porosity and fibre volume fraction and were produced by different processes, which makes the comparison difficult.

The damage threshold, which is generally not reported in the literature, is essential in order to compare different materials and to design thermostructural parts. The stress and strain at the damage threshold deduced from the tensile curves are 48 ± 8 MPa and 0.04 ± 0.01 %, respectively (see Table 2).

Cyclic loading tensile tests indicate low residual strains (see Fig. 9.a). The thermal residual stress and strain evaluated by the common intersection point method, established by Steen [20], are 63 MPa and 0.03 %. The hysteresis loops exhibited by the material indicate frictional sliding between fibres and matrix. Such a phenomenon could be expected in the studied material since the weak matrix enables fibre/matrix debonding, hence increasing frictional sliding.

3.2.2. Mechanical properties in ±45° fibre orientation

The response of the composite under monotonic tensile loading in ±45° fibre orientation shows a first linear segment, corresponding to the elastic region, and a curved second

segment (see Fig. 7). As reported in previous studies on different materials [8][18][21], Young's modulus (122 ± 28 GPa) and ultimate tensile strength (89 ± 19 MPa) in ±45° fibre orientation are lower than in the fibre direction (134 ± 19 GPa and 260 ± 37 MPa, respectively) and the material exhibits a greater capacity for inelastic straining in ±45° fibre orientation. The damage threshold (41 ± 11 MPa) is slightly lower in the off-axis direction, but the values are close to each other. Considering the weak matrix CMCs principle, it is obvious that the first damage occurs in the matrix and the damage threshold is expected to remain unchanged, regardless of the loading direction. Taking into account the scattering of the estimated thresholds in the fibre direction and in ±45° fibre orientation, these thresholds are consistent.

The in-plane shear modulus calculated from monotonic tensile tests in ±45° fibre orientation is 46 ± 12 GPa.

As in the fibre direction, cyclic loading tensile tests indicate low residual strains (see Fig. 9.b) and the material exhibits hysteresis loops. The area of these loops is slightly larger in this loading direction. This phenomenon can be attributed to a more extensive fibre/matrix debonding occurring for this fibre orientation. Indeed, as this will be developed in further section 3.3, fibre/matrix debonding occurs simultaneously for both fibre directions, warp and weft, when the composite is loaded in ±45° fibre orientation. Thus, there is more frictional sliding and the area of the hysteresis loops is larger in this direction than in the fibre direction.

3.2.3. Out-of-plane mechanical properties

The interlaminar shear strength of the composite, as measured by 3-point bending tests, is 20 ± 2 MPa. This value is higher than those reported by Simon [16] for Nextel™610/mullite composites (12.5 - 14 MPa) and Nextel™720/mullite composites (10 - 11.5 MPa). The material developed at Onera is thus expected to be more resistant to delamination than the composites described in the literature with lower interlaminar shear strengths.

3.3. Identification of the damage mechanisms

As aforementioned, the damage mechanisms of the material were studied through *post mortem* SEM observations and *in situ* SEM tensile testing; these complementary methods enabled to suggest the following damage scenario of the composite under tensile loading.

At early stage of loading, matrix cracking occurs. Considering the SEM observations on the as-processed material, it can be assumed that, when the damage threshold is reached, pre-existing matrix microcracks propagate while new cracks are initiated. Nevertheless, it is difficult to assess which phenomenon occurs first. The two phenomena probably occur simultaneously, depending on the local stress state in the material. We can also assume that the matrix cracking phenomenon starts at stresses lower than the apparent damage threshold (*i.e.* deduced from the stress-strain curves). In this case, early damage is not sufficient to induce a macroscopic loss of elasticity. Besides, matrix cracking occurs throughout loading, up to the composite failure. This phenomenon is clearly visible in the SEM micrographs (see Fig. 10) acquired during *in situ* tensile testing. According to Kostopoulos *et al.* [22] who identified the failure mechanisms in oxide/oxide composites using acoustic emission, matrix cracking occurs all along loading with an abrupt increase at a certain critical load.

Matrix cracks have two origins: *(i)* low strength of the microporous matrix and *(ii)* macroporosity. Indeed, macropores act as stress concentrators and, located in matrix-rich regions or in fibre tows (*i.e.* intraply macropores due to a lack of matrix), are responsible for crack initiation resulting in extensive matrix cracking. Crack initiation at macropores is visible in Fig. 11.a and Fig. 11.b, in specimens loaded to failure in fibre direction and in ±45° fibre orientation.

Matrix cracks then propagate in the matrix and are deflected at the fibre/matrix interface when reaching a fibre. This phenomenon is in accordance with weak matrix principle. Matrix cracks first propagate around the fibre tows (regardless of the loading direction, as observed in Fig. 11.a and Fig. 11.b), then in the fibre tows. When the fibres of a tow are not in contact,

cracks are not deviated around the tow but penetrate readily in the tow, as illustrated in Fig. 12.

Tow peripheral cracks, by debonding entire tows from the matrix, facilitate their movement within the matrix, leading to fibre extension. In the case of fibre direction loading, the extension of the longitudinal fibre tows leads to an increase in the undulation amplitude of the transversal tows. The internal stress system resulting from this phenomenon is responsible for interply matrix cracking which, considering fibre/matrix debonding in this weak matrix composite, contributes to delamination. According to Kostopoulos *et al.* [22], the disorientation and disruption of the woven reinforcement occurring after fibre/matrix debonding starts shortly before the composite final failure, when fibre failure becomes the dominant mechanism.

In the case of off-axis loading, the movement of the tows enhances in-plane shear in the different plies, thus increasing delamination. Regardless of the loading direction, the presence of interply macropores, revealed by SEM observations and X-ray tomography, enhances delamination.

After penetrating the fibre tows, cracks propagate within the tows, isolating the fibres from one another, especially in the case of load bearing tows.

Finally, failure occurs when the amount of fibres bearing the load is not sufficient. The damage mechanisms of the composite are illustrated in Fig. 13.

Nextel™610/alumina composite exhibits extensive pull-out and, in many cases, delamination. SEM observations of the fracture surface show that fibre failure events are uncorrelated (see Fig. 14), the distance between the fracture surfaces of different fibres belonging to the same tow attaining a few millimetres. This asserts the fact that the weak matrix allows separating the fibres from each other by fibre/matrix debonding within the tows. Levi *et al.* [1], Zok *et al.* [8] and Simon [16] reported the same phenomenon for other weak matrix oxide/oxide composites.

In this material, macropores, regardless of their dimension, seem to be the main cause of extensive matrix cracking, leading to a loss of stiffness of the composite. Nevertheless, inter-

and intraply macropores do not have the same effect, even though both act as stress concentrators. Intraply macropores are responsible for a loss of stiffness, increasing the strain capacity of the material, whereas interply macropores promote delamination, which makes them prejudicial to the 2D composites.

Besides the previous observations, it is noteworthy that the damage pattern is correlated to the direction of the reinforcement: cracks are parallel and perpendicular to the fibre tows, regardless of the loading direction.

4. Concluding remarks

The microstructure of Nextel™610/alumina composite was studied through several techniques, namely porosimetry, X-ray tomography and SEM observations, which appear to be complementary.

The as-processed material exhibits a heterogeneous microstructure. The composite is pre-damaged, showing shrinkage matrix microcracks and macropores. Two types of macropores can be differentiated: inter- and intraply macropores. The quality of as-processed plates and samples was assessed by X-ray tomography, infrared thermography and ultrasonic scanning techniques. These last two techniques provided similar information. However, infrared thermography inspection being faster, it thus appears to be the most suitable technique for initial damage detection.

An extensive study of the damage mechanisms of the composite, through *post mortem* SEM observations and *in situ* tensile testing in a SEM, showed that intraply macropores promote crack initiation, enabling energy dissipation and leading to a loss of stiffness, whereas interply macropores, acting as stress concentrators, promote delamination. In-plane and out-of-plane mechanical properties of the studied Nextel™610/alumina composite were higher than those reported in the literature. However, considering the difference in fibre volume fraction and porosity of the materials described in different studies, the comparison is rather difficult.

In order to avoid delamination in the Nextel™610/alumina composite, reducing the amount of interply macropores appears mandatory. This can be achieved by improving the manufacturing process in order to increase the cohesion between the plies. Enhancing fibre/matrix bonding could also restrain delamination, but it would also deteriorate the in-plane mechanical properties of the composite by limiting crack deflection at fibre matrix interface. Limiting the amount of macropores is currently under study at Onera.

The thermal *in situ* damage monitoring of the mechanical tests by passive thermography did not enable to visually locate the progressive damage of the tested oxide/oxide composite specimens. The late detection of damage, *i.e.* just before failure, may be attributed to the high amount of energy released by extensive fibre failure, whereas crack propagation in the matrix, occurring throughout loading, is not energetic enough to be detected. Random and isolated fibre failures occur during loading but the failure of a single filament is not energetic enough to be detected, contrary to the failure of entire tows which can be detected and lead to the specimen failure. The determination of the damage threshold of such materials will require an analysis of the local temperature evolution during mechanical loading.

Adapting other damage monitoring methods to oxide/oxide CMC is also currently under consideration.

Acknowledgements

The collaboration with *Herakles* is gratefully acknowledged. This work was supported under the PRC Composites, a French research project funded by *DGAC*, involving *Safran Group*, *Onera* and *CNRS*. The authors would like to thank *Safran Composites* for conducting X-ray tomography on our specimens. The authors are thankful to Dr. F. Laurin (Onera, DMSC) for developing the method of analysis of X-ray tomography data used in this study. The authors would like to thank M.-H. Ritti (Onera, DMSC) for her help in materials processing, F. Passilly, Dr. J.-M. Roche and Dr. B. Lamboul (Onera DMSC) for NDT inspections and A. Mavel (Onera, DMSC) for the mechanical testing of the specimens. The authors are also

grateful to D. Boivin, Y. Renollet and N. Horezan (Onera, DMSM) who co-developed and conducted SEM *in situ* testing, and to M. Bejet (Onera, DMSC) who designed specific jaws adapted to the *in situ* tensile testing of parallelepipedic shaped composite specimens.

References

1. Levi CG, Yang JY, Dalgleish BJ, Zok FW, Evans AG. Processing and performance of an all-oxide ceramic composite. Journal of the American Ceramic Society. 1998;81:2077-2086.

2. Jackson PR, Ruggles-Wrenn MB, Baek SS, Keller KA. Compressive creep behavior of an oxide-oxide ceramic composite with monazite fiber coating at elevated temperatures. Materials Science and Engineering A. 2007;454-455:590-601.

3. Ruggles-Wrenn MB, Radzicki AT, Baek SS, Keller KA. Effect of loading rate on the monotonic tensile behavior and tensile strength of an oxide-oxide ceramic composite at 1200°C. Materials Science and Engineering A. 2008;492:88-94.

4. Ruggles-Wrenn MB, Szymczak NR. Effects of steam environment on compressive creep behavior of N720/alumina ceramic composite at 1200°C. Composites Part A. 2008;39:1829-1837.

5. Ruggles-Wrenn MB, Mall S, Eber CA, Harlan LB. Effects of steam environment on high-temperature mechanical behavior of Nextel™720/alumina (N720/A) continuous fiber ceramic composite. Composites Part A. 2006;37:2029-2040.

6. Parlier M, Ritti MH. State of the art and perspectives for oxide/oxide composites. Aerospace Science and Technology. 2003;7:211-221.

7. Cantonwine PE. Strength of thermally exposed alumina fibers. Part II Bundle behavior. Journal of Materials Science. 2003;38:471-480.

8. Zok FW, Levi CG. Mechanical properties of porous-matrix ceramic composites. Advanced Engineering Materials. 2001;3:15-23.

9. Koch D, Tushtev K, Grathwohl G. Ceramic fiber composites: Experimental analysis and modeling of mechanical properties. Composites Science and Technology. 2008;68:1165-1172.

10. Holmquist MG, Lange FF. Processing and properties of a porous oxide matrix composite reinforced with continuous oxide fibers. Journal of the American Ceramic Society. 2003;86:1733-1740.

11. Mattoni MA, Yang JY, Levi CG, Zok FW. Effects of matrix porosity on the mechanical properties of a porous-matrix, all-oxide ceramic composite. Journal of the American Ceramic Society. 2001;84:2594-2602.

12. Wilson DM, Visser LR. High performance oxide fibers for metal and ceramic composites. Composites Part A. 2001;32:1143-1153.

13. Kerans RJ, Hay RS, Parthasarathy TA. Structural ceramic composites. Current Opinion in Solid State and Materials Science. 1999;4:445-451.

14. Parlier M, Ritti MH, Jankowiak A. Potential and perspectives for oxide/oxide composites. Journal Aerospace Lab. 2011;AL3-09.

15. Ben Ramdane C. Etude et modélisation du comportement mécanique de CMC oxyde/oxyde, Ph.D. dissertation (in french), Université de Bordeaux. 2014.

16. Simon RA. Progress in processing and performance of porous-matrix oxide-oxide composites. International Journal of Applied Ceramic Technology. 2005;2(2):141-149.

17. Ruggles-Wrenn MB, Musil SS, Mall S, Keller, KA. Creep behavior of Nextel™610/monazite/alumina composite at elevated temperatures. Composites Science and Technology. 2006;66:2089-2099.

18. Zawada LP, Hay RS, Lee SS, Staehler J. Characterization and high-temperature mechanical behavior of an oxide/oxide composite. Journal of the American Ceramic Society. 2003;86(6):981-990.

19. Jurf RA, Butner SC. Advances in oxide-oxide CMC. Journal of Engineering for Gas Turbines and Power. 2000;122:202-205.

20. Steen M. Tensile mastercurve of ceramic matrix composites: significance and implications for modelling. Materials Science and Engineering A. 1998;250:241-248.

21. Heathcote JA, Gong XY, Yang JY, Ramamurty U, Zok FW. In-plane mechanical properties of an all-oxide ceramic composite. Journal of the American Ceramic Society. 1999;82:2721-2730.

22. Kostopoulos V, Loutas TH, Kontsos A, Sotiriadis G, Pappas YZ. On the identification of the failure mechanisms in oxide/oxide composites using acoustic emission. NDT&E International. 2003;36:571-580.

Figures:

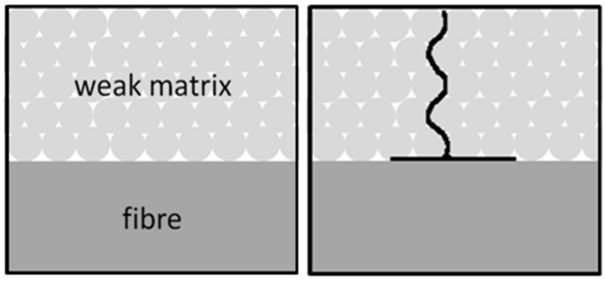

Fig. 1. Schematic diagram of crack deflection at the fibre/matrix interface in a weak matrix CMC.

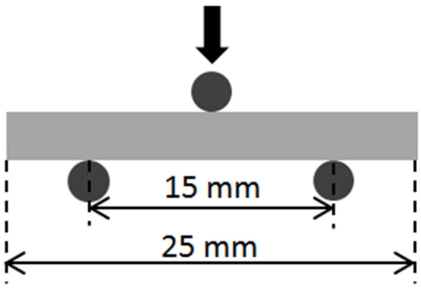

Fig. 2. Schematic diagram of the 3-point bending test geometry for the determination of interlaminar shear strength.

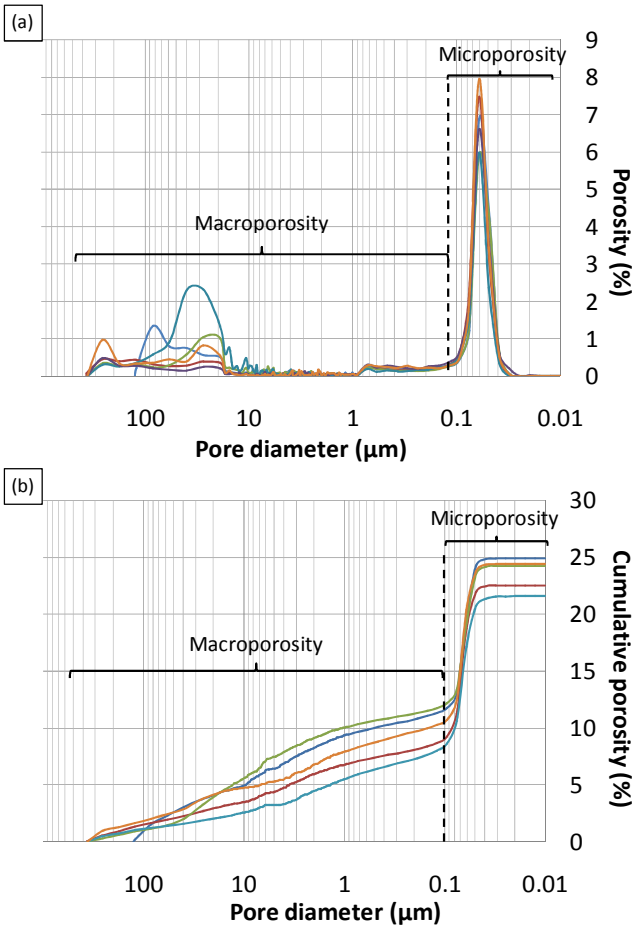

Fig. 3. Pore size distribution as determined by mercury intrusion porosimetry. a. Porosity vs. pore diameter. b. Cumulative porosity vs. pore diameter.

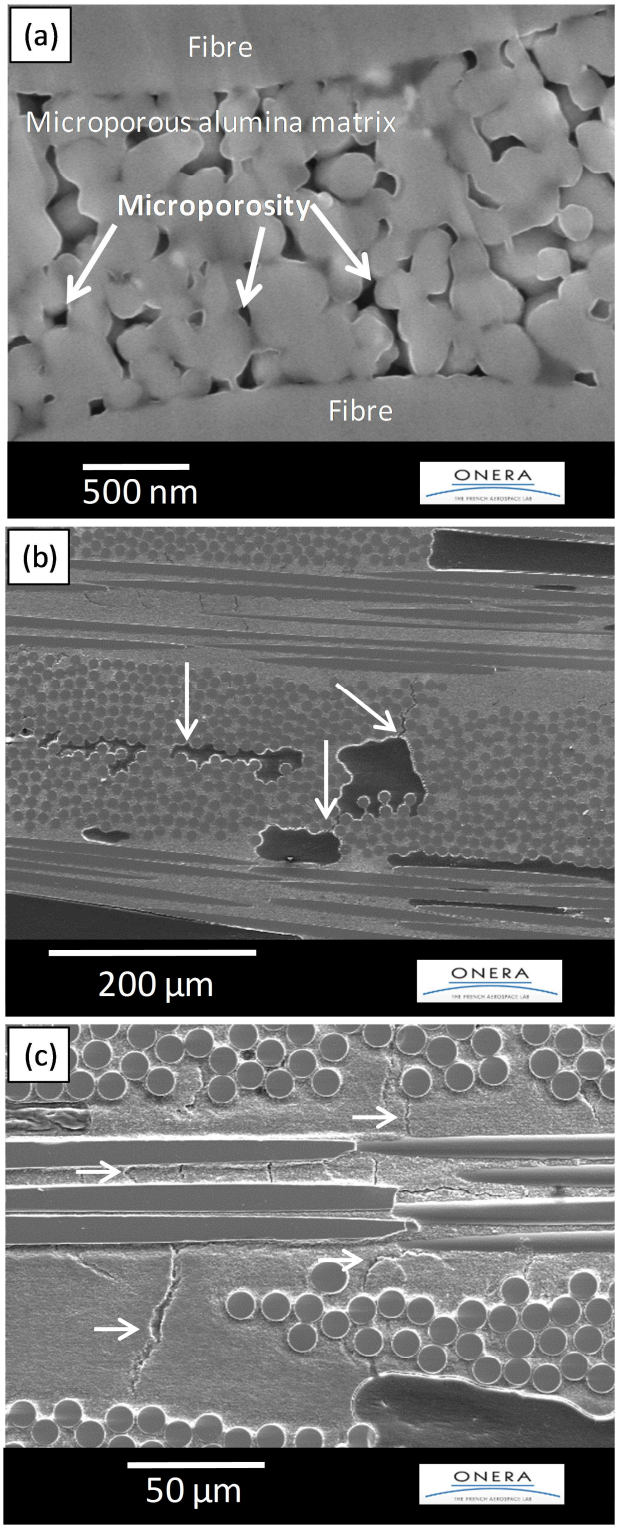

Fig. 4. SEM observations of as-processed Nextel™610/alumina composite. a. Microporosity of the matrix, enabling crack deflection at the fibre/matrix interface (ion polishing). b. Intraply macropores, due to a lack of matrix, and crack initiation at macropores. c. Sintering shrinkage matrix cracks, perpendicular to the plies.

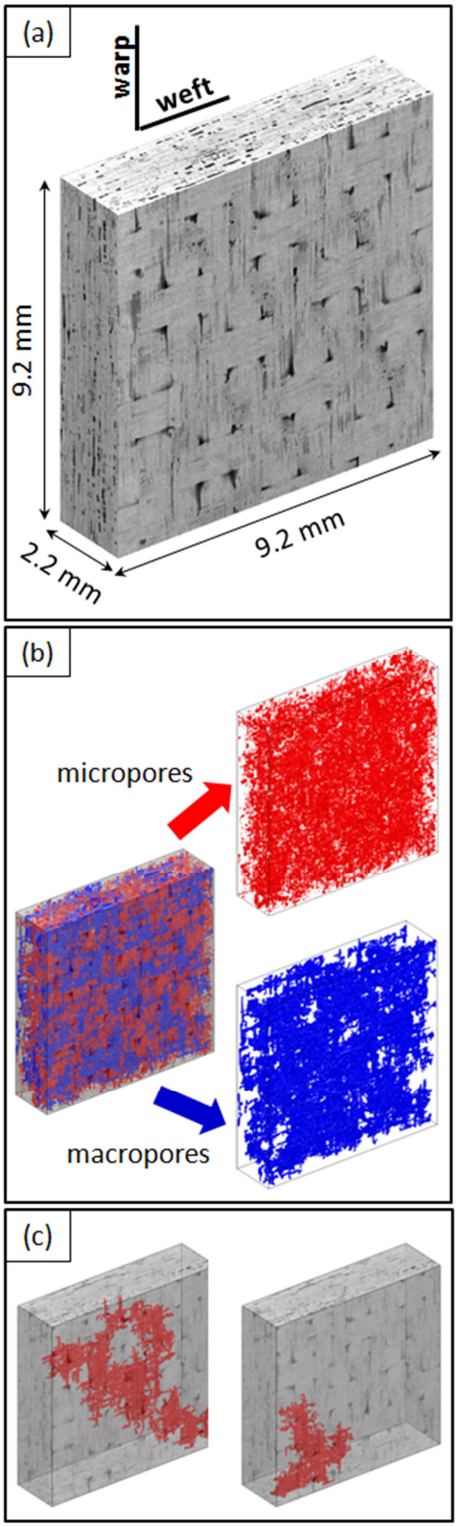

Fig. 5. X-Ray tomography analysis of Nextel™610/alumina composite. a. Reconstruction of the zone of interest. b. Distinction between macro- and micropores. c. Example of the two largest macropores of the zone of interest.

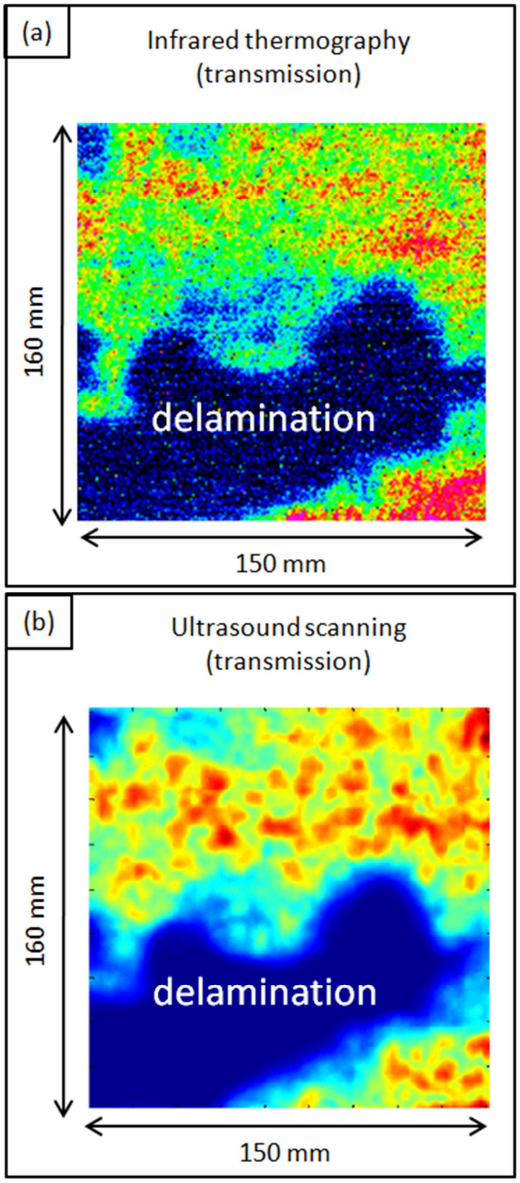

Fig. 6. Example of a plate showing intensive delamination as established through a. infrared thermography and b. ultrasonic scanning inspection. The results obtained by the two techniques are similar.

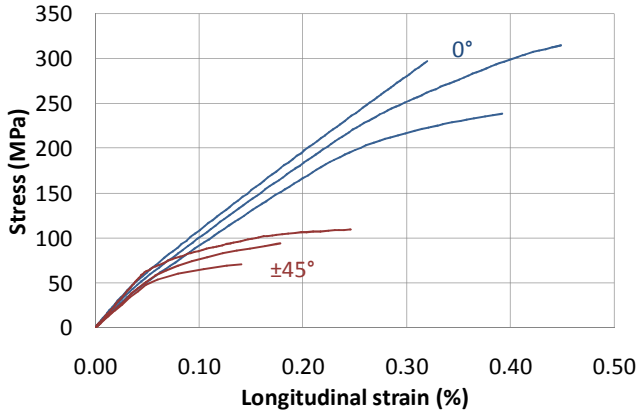

Fig. 7. Stress-strain curves of Nextel™610/alumina composite under tensile loading in 0° and ±45° fibre orientations. For each loading direction, extreme and average curves are represented.

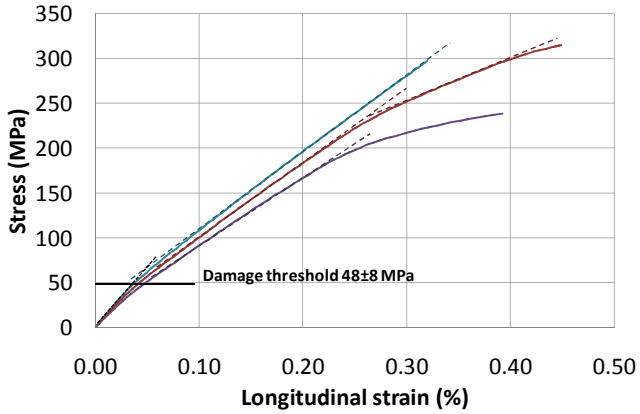

Fig. 8. Stress-strain curves of Nextel™610/alumina composite under tensile loading in 0° fibre direction: distinction between the different domains of the curves, namely the elastic domain (first linear part), the second linear part and, in some cases, the third part (generally non linear). The damage threshold is determined as the end of the elastic domain.

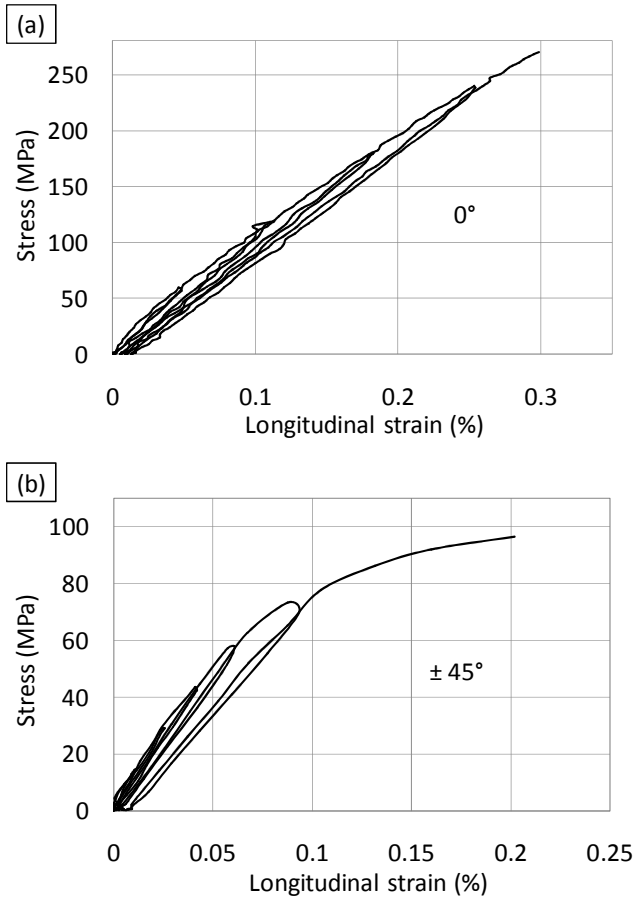

Fig. 9. Stress-strain curves of Nextel™610/alumina composite under cyclic tensile loading in a. 0° fibre direction and b. ±45° fibre orientation.

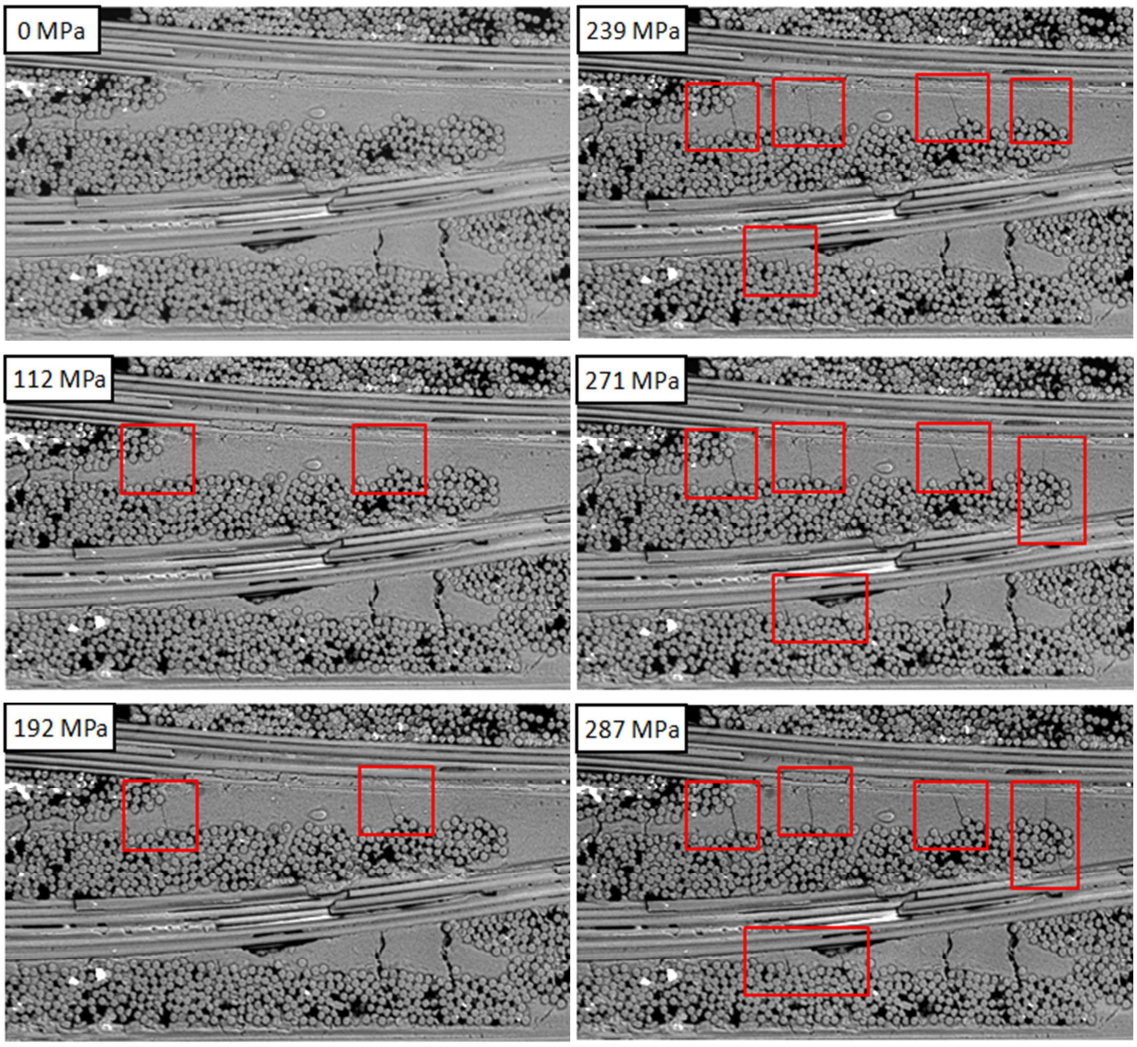

Fig. 10. *In situ* SEM observations of Nextel™610/alumina composite under tensile loading: matrix crack opening and propagation throughout loading. At elevated load, matrix cracks span the transverse fibre tows.

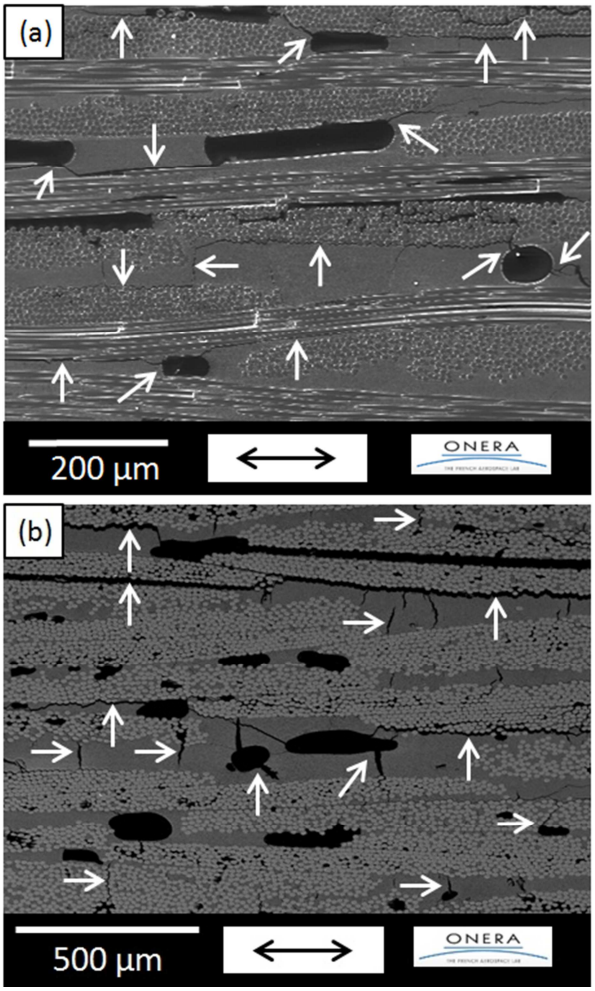

Fig. 11. SEM observations of Nextel™610/alumina composites tensile tested to failure. a. Longitudinal section of a specimen loaded in the fibre direction: matrix cracks perpendicular to the plies deflected at the fibre/matrix interface, crack initiation at macropores. b. Longitudinal section of a specimen loaded in ±45° fibre orientation: matrix cracks perpendicular to the plies deflected at the fibre/matrix interface, crack initiation at macropores.

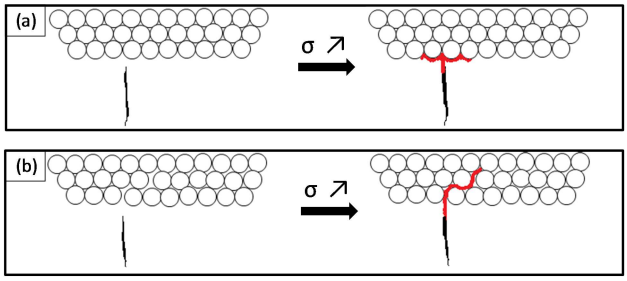

Fig. 12. Schematic diagram of the deflection of a matrix crack arriving on a fibre tow when a. the fibres are in contact or b. the fibres are separated by the matrix.

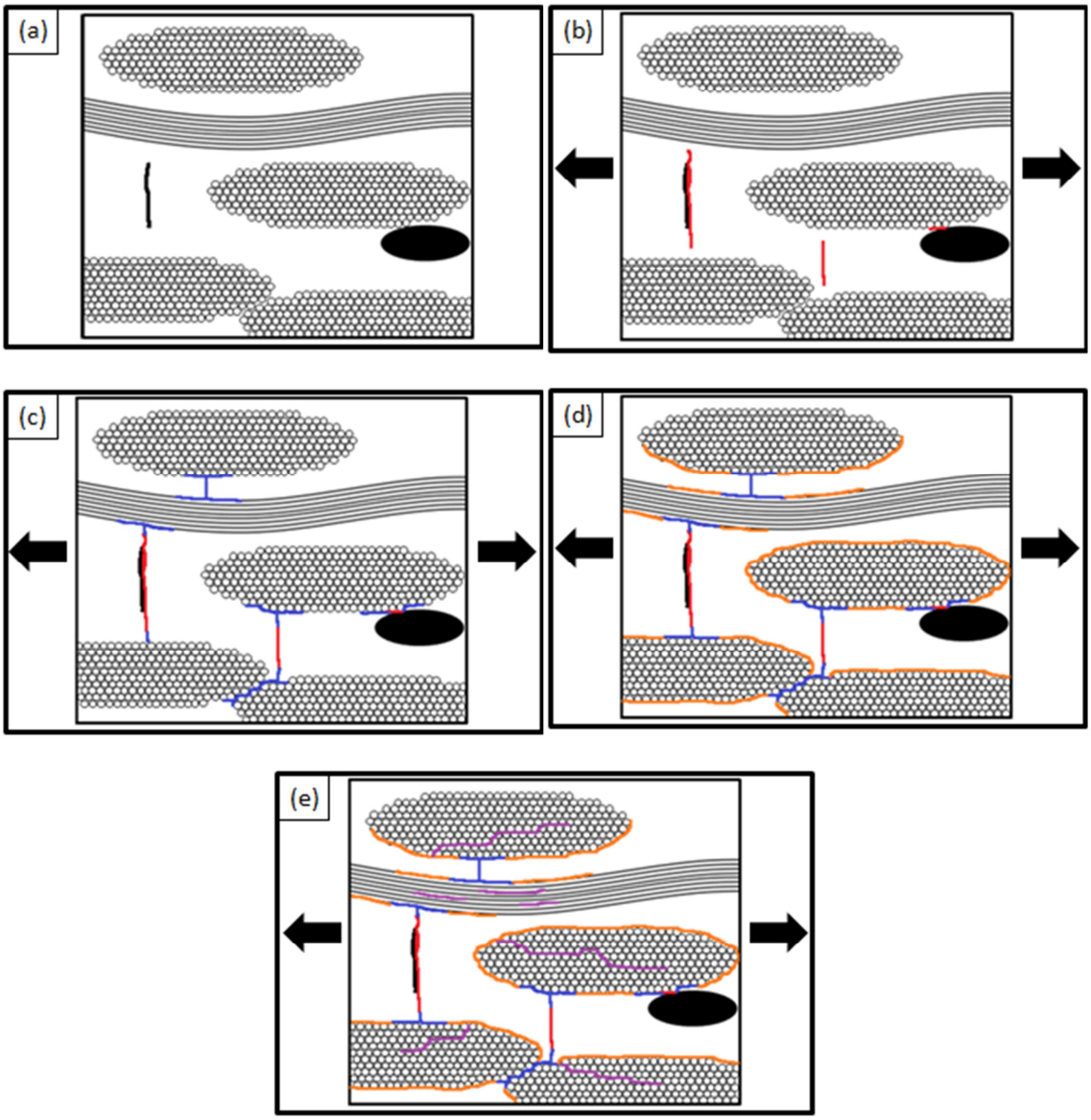

Fig. 13. Schematic diagrams of the damage mechanisms of Nextel™610/alumina weak matrix composite subjected to tensile loading. a. As-processed material, showing a macropore and a sintering matrix crack. b. Opening of the pre-existing matrix crack, matrix cracking, crack initiation phenomenon at the macropore. c. Crack deflection at the tow/matrix interface. d. Propagation of the deflected cracks around the fibre tows. e. Crack propagation within the fibre tows.

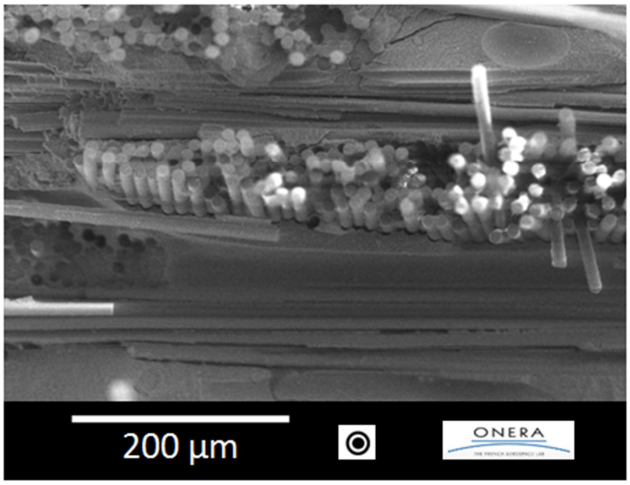

Fig. 14. Fractography of a specimen loaded in the fibre direction: the single filaments belonging to the same tow are separated, resulting from intensive fibre/matrix debonding within the tow.

Tables:

Total porosity (%)	24 ± 2
Fibre volume fraction (%)	49 ± 0
Macroporosity (%)	12 ± 1
Microporosity (%)	13 ± 1
Matrix porosity (%)	32 ± 1

Table 1. Porosity and fibre volume fraction as determined by mercury intrusion porosimetry (five samples from five different plates).

	Ultimate stress (MPa)	Longitudinal strain at ultimate stress (%)	Damage threshold stress * (MPa)	Strain at damage threshold stress (%)	Young's modulus * (GPa)	In-plane shear modulus (GPa)
Tensile tests 0° : 9 specimens, 6 plates	260 ± 37	0.30 ± 0.09	48 ± 8	0.04 ± 0.01	134 ± 19	
Tensile tests ±45°: 7 specimens, 3 plates	89 ± 19	0.19 ± 0.07	41 ± 11	0.04 ± 0.02	122 ± 28	46 ± 12

* determination on the stress-strain curves

Table 2. Mechanical properties of Nextel™610/alumina composite subjected to tensile loading in the fibre direction and in ±45° fibre orientation.